Jammed Particle Configurations and Dynamics in High-Density Lennard-Jones Binary Mixtures in Two Dimensions

Hayato Shiba[1] and Akira Onuki[2]

[1]*Institute for Solid State Physics, University of Tokyo, Chiba 277-8581, Japan*
[2]*Department of Physics, Kyoto University, Kyoto 606-8502, Japan*

We examine the changeover in the particle configurations and the dynamics in dense Lennard-Jones binary mixtures composed of small and large particles. By varying the composition at a low temperature, we realize crystal with defects, polycrystal with small grains, and glass with various degrees of disorder. In particular, we show configurations where small crystalline regions composed of the majority species are enclosed by percolated amorphous layers composed of the two species. We visualize the dynamics of configuration changes using the method of bond breakage and following the particle displacements. In quiescent jammed states, the dynamics is severely slowed down and is highly heterogeneous at any compositions. In shear, plastic deformations multiply occur in relatively fragile regions, growing into large-scale shear bands where the strain is highly localized. Such bands appear on short time scales and change on long time scales with finite life times.

§1. Introduction

Binary particle systems with size dispersity exhibit complicated phase behavior depending on the temperature T, the average number density $n = (N_1 + N_2)/V$, and the composition $c = N_2/(N_1 + N_2)$.[1)–6)] Here N_1 and N_2 are the numbers of the small and large particles in a volume V, respectively. At high densities, the particle configurations sensitively depend on the size ratio σ_2/σ_1 between the diameters of the two species, σ_1 and σ_2. If σ_2/σ_1 is close to unity at large n and at low T, a crystal state is realized with a small number of defects. However, if σ_2/σ_1 considerably deviates from unity, crystal states are realized only for very small c or $1-c$. For not small c and $1-c$, polycrystal and glass states emerge without long-range crystalline order at low T. It is then of great interest how the particle configurations and the dynamics change with varying the composition c at considerably large size dispersity. As the glass transition is approached, the structural relaxation time $\tau_\alpha(T)$ grows dramatically from a microscopic to macroscopic time, while the particle configurations remain random yielding the structure factors similar to those in liquid.

The dynamics of supercooled liquid and glass have been studied extensively using molecular dynamics simulations (MD). As a marked feature, the glass dynamics is highly heterogeneous.[7)–16)] In particular, Yamamoto and one of the present authors[10)] examined breakage of appropriately defined bonds. The broken bonds accumulated in long time intervals are analogous to the critical fluctuations in Ising systems such that their structure factor may be fitted to the Ornstein-Zernike form,

$$S_{\rm b}(k) = S_{\rm b}(0)/(1 + k^2\xi^2), \tag{1}$$

in two dimensions (2D) and in three dimensions (3D). The wave number k is smaller than the inverse particle size. The correlation length ξ can thus be determined,

which grows with lowering T. Bond breakage events tend to take place repeatedly in relatively fragile regions, leading to aggregation of broken bonds on long time scales. Kob *et al.*[11] pointed out relevance of stringlike clusters of mobile particles whose lengths increase at low T. In addition, the diffusion constant in glassy materials is strongly affected by the dynamic heterogeneity.[17)–19)] Afterwards, some authors have claimed the presence of correlation between the structural heterogeneity in the particle configurations and the dynamic heterogeneity on long time scales.[13)–15)] Recently significant heterogeneity has been found in the elastic moduli in glass,[20),21)] which is the origin of nonaffine elastic displacements for very small strains.

Glass dynamics under shear flow has also been studied by many authors,[22)–31)] where the shear rate $\dot{\gamma}$ is a new parameter representing the degree of nonequilibrium. Similar jamming rheology has been found in foam and microemulsion systems, colloid suspensions, and granular materials.[32)–36)] In jammed states of molecular glass, each particle undergoes shear-induced configuration changes on the time scale of $\dot{\gamma}^{-1}$. At a low temperature T, the total rate of the configuration change is given by[22),23)]

$$\tau_\alpha(T,\dot{\gamma})^{-1} = \tau_\alpha(T)^{-1} + A_\alpha\dot{\gamma}. \tag{2}$$

In the right hand side, the first term is the thermal activation rate and the second one is the shear-induced rate, where the coefficient A_α is of order unity. The steady-state viscosity $\eta(T,\dot{\gamma})$ is proportional to $\tau_\alpha(T,\dot{\gamma})$. The following dynamic scaling relation for the correlation length was in accord with the simulation:[10),22)]

$$\xi(T,\dot{\gamma}) \sim \tau_\alpha(T,\dot{\gamma})^{1/z}, \tag{3}$$

including the sheared case. The dynamic exponent z was estimated as 4 in 2D and 2 in 3D. In glass a Weissenberg number may be defined by

$$\mathrm{Wi} = \tau_\alpha(T)\dot{\gamma}. \tag{4}$$

A nonlinear response regime emerges for Wi>1. Around the glass transition, $\tau_\alpha(T)$ grows and the regime Wi$\gg 1$ is realized even for extremely small shear, where the configuration change is mostly induced by shear and $\eta \sim \dot{\gamma}^{-1}$. Indeed in this condition, shear-thinning behavior was measured in glass under uniaxial stress.[37),38)] Also for near-critical and complex fluids, the criterion of nonlinear shear effects is given by Wi$=\tau\dot{\gamma} > 1$ with an appropriate long relaxation time τ.[39)] Moreover, a number of MD simulations of sheared glass have realized self-organization of "shear bands" with high strain localization extending througout the system. In simple shear flow such bands are nearly along the flow or the velocity-gradient direction,[25),29)–31)] while under uniaxial stress they make an angle of $\pi/4$ with respect to the uniaxial axis.[40)–44)] In metallurgy, shear bands have been observed in amorphous solids under uniaxial stretching or compression above a yield stress.[45)–47)]

Plastic deformations in crystal and polycrystal are extremely complex and are still poorly understood despite their extensive research.[48)–56)] In crystal with low-density defects, dislocation motions play a major role in plasticity, where they yield slip planes with various sizes as observed in acoustic emission experiments[49)] and by transmission electron microscopy.[50)] In polycrystal, the particles in the vicinity

of grain boundaries are relatively mobile compared to those within the grains, so their collective motions give rise to sliding of the grain boundaries under applied stress.[54)–56)] In these systems, plastic events take place as bursts or avalanches spanning wide ranges of space and time scales. In this manner, they intermittently release the elastic energy stored in the crystalline regions at high strain. On the other hand, in glass under stress, plastic events have been assumed to be spatially localized due to the structural disorder in glass,[57)–59)] but our recent 2D simulation has shown that they frequently take place over wide areas in short times.[31)] In glass, slip elements (slip lines in 2D) do not much exceed the particle size, but they successively appear in their neigborhood forming large-scale aggregates. When glass rheology is studied in simulation, such avalanches manifest themselves in large stress drops in the stress-strain curve. The irregularity of the average stress versus time has been conspicuous in numerous simulations in the literature, even though the curve should become smoother with increasing the system size. Molecular glassy materials behave as elastic bodies on short time scales with mesoscopically inhomogeneous elastic moduli.[20),21)] Thus large-scale release of the elastic energy at high stress is a common feature of plasticity in crystal, polycystal, and glass.

In this paper, we will investigate the heterogeneity dynamics in high-density and low-temperature 2D model binary mixtures without and with applied shear for various compositions on the basis of our previous work.[6),14),56)] We are interested in the relationship between the dynamic heterogeneity on long time scales and the structural heterogeneity in the particle configurations. In a separate paper we have examined rheology and plastic deformations on various time scales.[31)]

The organization of this paper is as follows. In Sec.II, our model and our simulation method will be explained. In Sec.III, numerical results will be presented on the particle configurations and the heterogeneous dynamics for various c without shear. In Sec.IV, we will examine the collective dynamics under shear, which are even more heterogeneous than in quiescent states.

§2. Background of Simulation

2.1. *Model*

Our two-dimensional (2D) binary mixtures[6),14),56)] consist of two species 1 and 2 interacting via truncated Lennard-Jones (LJ) potentials,

$$v_{\alpha\beta}(r) = 4\epsilon \left[\Big(\frac{\sigma_{\alpha\beta}}{r}\Big)^{12} - \Big(\frac{\sigma_{\alpha\beta}}{r}\Big)^{6} \right] - C_{\alpha\beta} \tag{5}$$

which are characterized by the energy ϵ and the interaction lengths $\sigma_{\alpha\beta} = (\sigma_\alpha + \sigma_\beta)/2$ $(\alpha, \beta = 1, 2)$. The $r = |\boldsymbol{r}_j - \boldsymbol{r}_k|$ is the particle distance. Hereafter $\boldsymbol{r}_j$ denote the particle positions. The diameters of the two species are σ_1 and σ_2 and their ratio is fixed at $\sigma_2/\sigma_1 = 1.4$. For $r > r_{\rm cut} = 3.2\sigma_1$, we set $v_{\alpha\beta} = 0$ and the constant $C_{\alpha\beta}$ ensures the continuity of $v_{\alpha\beta}$ at $r = r_{\rm cut}$. The particle number is $N = N_1 + N_2 = 9000$ and the composition $c = N_2/N$ is varied. The system is in the region $-L/2 < x, y < L/2$. The volume L^2 is chosen such that the volume fraction of the soft-core regions is fixed as $(N_1\sigma_1^2 + N_2\sigma_2^2)/L^2 = 1$. We integrated the equations

of motion using the leapfrog method, where the time step is 0.002τ with

$$\tau = \sigma_1\sqrt{m_1/\epsilon}. \tag{6}$$

The mass ratio is fixed at $m_1/m_2 = (\sigma_1/\sigma_2)^2$. The following data were taken at $T = 0.2\epsilon/k_B$. The space coordinates x and y, the time t, the shear rate $\dot{\gamma}$, and the temperature T will be measured in units of σ_1, τ, τ^{-1}, and ϵ/k_B, respectively.

There was no tendency of phase separation in our simulation. For the parameters we adopt in this paper, the structural relaxation time $\tau_\alpha(T, c)$ without shear is of order 10^4 in glass, is longer in polycrystal, and tends to infinity in crystal from the decay of the self-time-correlation function.[14] The grain boundary motions are severely slowed down in the presence of large size dispersity, while they move rather fast in one-component systems. Thus τ_α is longer in polycrystal than in glass.

2.2. *Orientation angle and disorder variable*

In the particle configurations at high density, a large fraction of the particles are enclosed by six particles. The local crystalline order may then be represented by a sixfold orientation.[60] We define an orientation angle α_j in the range $-\pi/6 \le \alpha_j < \pi/6$ for each particle $j \in \alpha$ using the complex number,[6),14),56)]

$$\Psi_j = \sum_{k\in\text{bonded}} \exp[6i\theta_{jk}] = |\Psi_j|e^{6i\alpha_j}, \tag{7}$$

where the summation is over the "bonded" particle $k \in \beta$ satisfying $r_{jk} = |\boldsymbol{r}_j - \boldsymbol{r}_k| < 1.5\sigma_{\alpha\beta}$. The θ_{jk} is the angle of the relative vector $\boldsymbol{r}_j - \boldsymbol{r}_k$ with respect to the x axis.

We also introduce another non-negative-definite variable, called the disorder variable, which represents the degree of the deviation from the hexagonal order for each particles j by

$$D_j = \sum_{k\in\text{bonded}} |e^{6i\alpha_j} - e^{6i\alpha_k}|^2 = 2\sum_{k\in\text{bonded}} [1 - \cos 6(\alpha_j - \alpha_k)]. \tag{8}$$

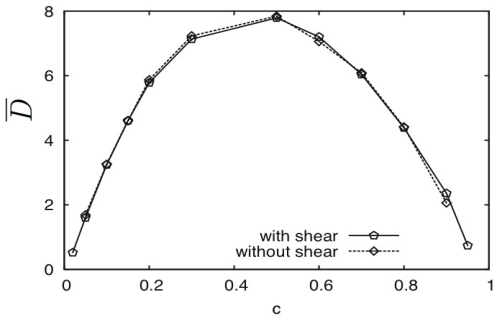

Fig. 1. Average disorder variables $\bar{D}$ vs c without shear and with shear $\dot{\gamma} = 10^{-4}$, where $T = 0.2$ and $N = 9000$.

Here D_j are in the range 15-20 for particles around defects, while $D_j \cong 0$ for a perfect crystal at low T. The degree of the overall disorder may be represented by the average over the particles,[6)]

$$\bar{D} = \sum_{j=1}^{N} D_j/N, \tag{9}$$

which is large in glass and liquid and is small in crystal. In Fig. 1, we show the average $\bar{D}$ versus c at $T = 0.2$ without shear and with shear $\dot{\gamma} = 10^{-4}$, where the two curves nearly coincide. For this shear rate (much smaller than

the molecular frequency τ^{-1}), there is no proliferation of defects induced by shear, while the defect structure is continuously deformed by shear. The maximum of $\bar{D}$ is attained at $c \sim 0.5$. See Figs. 8 and 9 of Ref. 6 for $\bar{D}$ as a function of T and σ_2/σ_1.

The angle variable α_j was originally introduced to study the thermal fluctuations of the hexagonal lattice structure around the melting transition in 2D.[60] We have recently studied 2D melting numerically with the aid of visualization of α_j and D_j,[61] where polycrystalline patterns are apparent at the melting not in accord with the original theory[60] (see the end of the last section for more discussions).

2.3. *Bond breakage*

The jamming dynamics can be conveniently visualized if use is made of the bond breakage.[10),22)] For each particle configuration at a time t, a pair of particles $i \in \alpha$ and $j \in \beta$ is considered to be bonded if

$$r_{ij}(t) = |\boldsymbol{r}_i(t) - \boldsymbol{r}_j(t)| \leq A_1 \sigma_{\alpha\beta}, \tag{10}$$

where $\sigma_{\alpha\beta} = (\sigma_\alpha + \sigma_\beta)/2$. We set $A_1 = 1.2$; then, $A_1\sigma_{\alpha\beta}$ is slightly larger than the peak distance of the pair correlation functions $g_{\alpha\beta}(r)$. After a time interval Δt, the bond is regarded to be broken if

$$r_{ij}(t + \Delta t) \geq A_2 \sigma_{\alpha\beta}, \tag{11}$$

where we set $A_2 = 1.5$. In the following figures, bonds broken during a time interval $[t_1, t_2]$ will be marked by $\times$ at the middle point $\boldsymbol{R}_{ij} = \frac{1}{2}(\boldsymbol{r}_i(t_2) + \boldsymbol{r}_j(t_2))$ of the two particle positions at the terminal time t_2. The structure factor of these middle points is written as $S_b(k)$ in Eq.(1).

In the original simulation using the soft-core potential,[10),22)] the bond breakage rate was $\tau_b(T, \dot{\gamma})^{-1} \cong 0.1\tau_\alpha(T, \dot{\gamma})^{-1}$, where $\tau_\alpha(T, \dot{\gamma})$ is the decay time of the self-correlation function and behaves as in Eq.(2) in shear. The $\tau_b(T, \dot{\gamma})$ represents the average bond life time and the broken bond number ΔN_b of the whole system is of order $N\tau_b(T, \dot{\gamma})^{-1}\Delta t$ in time interval Δt. For Wi> 1, the bond breakage is mostly induced by shear and the time average of the broken bond number per particle $\Delta N_b/N$ is of the order of the average strain $\dot{\gamma}\Delta t$ in the plastic flow regime. Around this mean value, $\Delta N_b/N$ increases significantly on occurrences of large-scale plastic events and decreases in "elastic periods" without them.[31)]

2.4. *Averaged velocity*

Shear bands have been observed widely in complex fluids, glassy fluids, and granular materials. To examine such strain localization in shear flow, we may introduce an averaged velocity $\bar{v}_x(y, t)$ as follows.[31)] We first integrate the x component of the momentum density $J_x(x, y, t)$ in the flow direction:

$$\bar{J}_x(y, t) = \frac{1}{L}\int_{-L/2}^{L/2} dx J_x(x, y, t) = \frac{1}{L}\sum_j m_j \dot{x}_j(t)\delta(y - y_j(t)). \tag{12}$$

We next smooth $\bar{J}_x(y, t)$ over space and time intervals with widths Δy and Δt as

$$\bar{v}_x(y, t) = \frac{1}{\bar{\rho}\Delta y \Delta t}\int_{y-\Delta y/2}^{y+\Delta y/2} dy' \int_t^{t+\Delta t} dt' \bar{J}_x(y', t'), \tag{13}$$

where $\bar{\rho}$ is the average mass density. We fix Δy at $L/20$. However, we choose Δt depending on the time scale of plastic events under consideration. This is because of the hierarchical dynamics of plastic deformations.

§3. Numerical results in quiescent states

Without applied shear, we first integrated the equations of motion under the periodic boundary conditions in the x and y directions. We equilibrated the system at $T = 0.2$ for a time interval of 5×10^3 until no appreciable time evolution was detected in various thermodynamic quantities. At this time we will set $t = 0$. We attached a Nosè-Hoover thermostat[62),63)] to all the particles, which then obeyed

$$m_j \ddot{\boldsymbol{r}}_j = -\frac{\partial}{\partial \boldsymbol{r}_j} U - \zeta m_j \dot{\boldsymbol{r}}_j, \tag{14}$$

where $\dot{\boldsymbol{r}}_j = d\boldsymbol{r}_j/dt$, $\ddot{\boldsymbol{r}}_j = d^2\boldsymbol{r}_j/dt^2$, and U is the total potential. The thermostat variable $\zeta(t)$ obeyed

$$\frac{d}{dt}\zeta = \frac{1}{\tau_{\rm NH}^2}\left[\frac{1}{NT}\sum_j \frac{m_j}{2}\dot{\boldsymbol{r}}_j^2 - 1\right], \tag{15}$$

where $\tau_{\rm NH}$ is the thermostat characteristic time. We set $\tau_{\rm NH} = 0.961$.

By varying c in the range $c \leq 0.5$ at $\sigma_2/\sigma_1 = 1.4$, Hamanaka and one of the present authors[6),14)] realized crystal states with small numbers of defects for

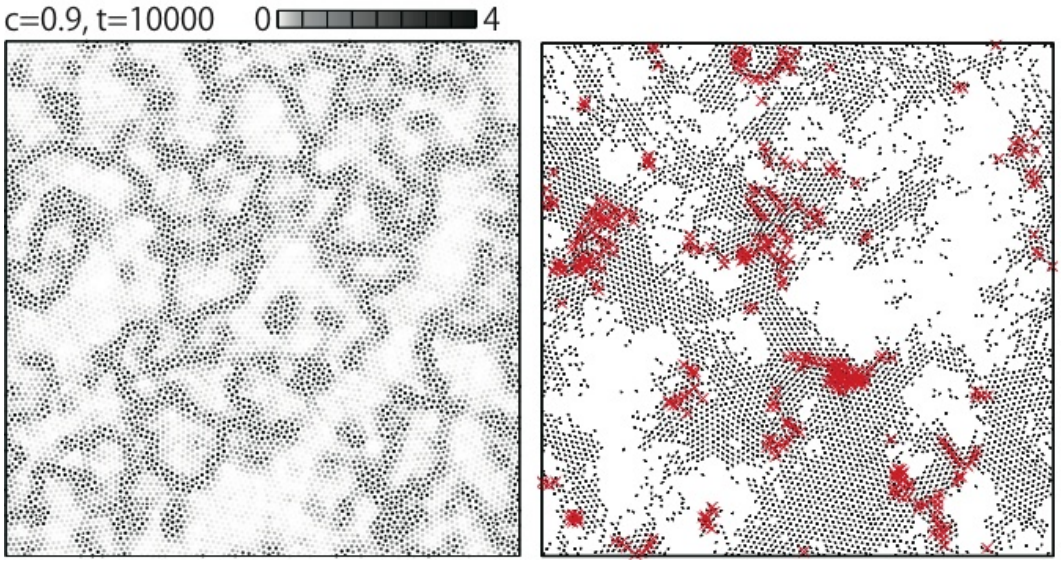

Fig. 2. (color online) Left: disorder variables $D_j(t)$ at $t = 10^4$ with the gradation bar at the top, where $\dot{\gamma} = 0$ and $c = 0.9$. Crystalline regions composed of the large particles (white) are enclosed by percolated amorphous layers containing the small particles (gray or black). Right: broken bonds ($\times$) and displacement vectors for mobile particles with $|\Delta \boldsymbol{r}_j| > 0.2$ in the time interval $[10^4, 4 \times 10^4]$ with width $\Delta t = 3 \times 10^4$ in the same run. The particles with $D_j > 4$ are written in black (left). The whole system $-L/2 < x, y < L/2$ is shown.

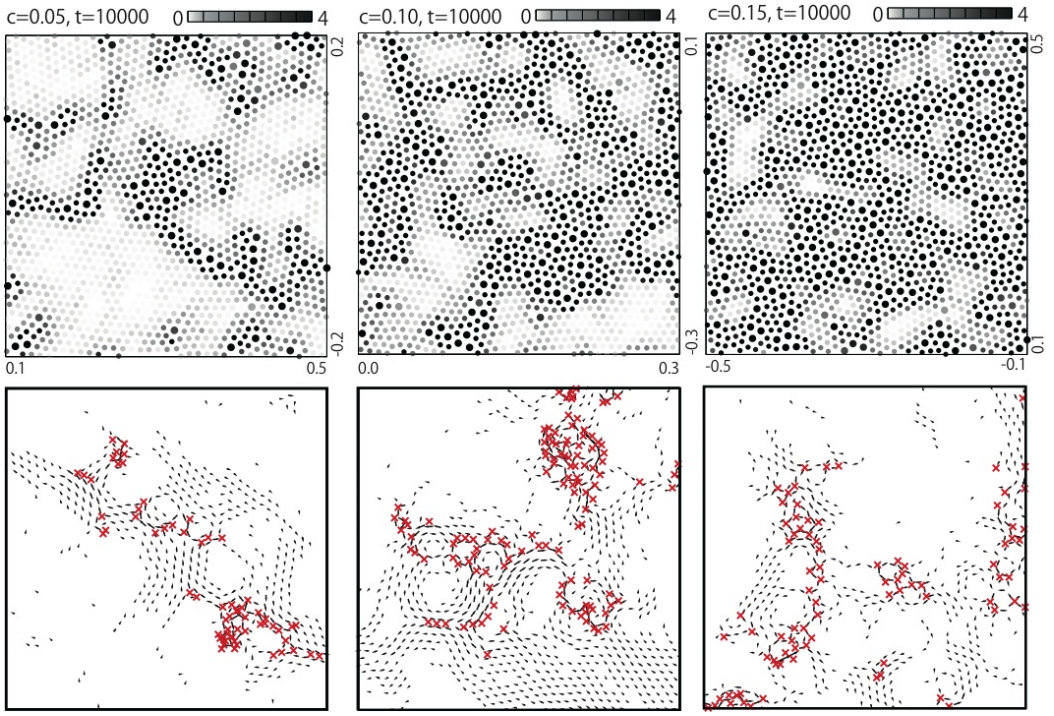

Fig. 3. (color online) Upper plates: disorder variables $D_j(t)$ at $t = 10^4$ for $c = 0.05$, 0.1, and 0.15 with $\dot{\gamma} = 0$. Lower plates: broken bonds ($\times$) and displacement vectors for mobile particles with $|\Delta \boldsymbol{r}_j| > 0.2$ in the time interval $[10^4, 4\times10^4]$ in the same run producing the corresponding upper panel. These are snapshots of 1/16 of the total system. The numbers at the corners (upper plates) denote the normalized coordinate x/L or y/L.

$c \lesssim 0.01$, polycrystal states with the large particles forming grain boundaries for $0.01 \lesssim c \lesssim 0.12$, and glass states for larger c. For $c \gtrsim 0.1$, the system is divided into small crystalline domains composed of the small particles and percolated amorphous regions composed of the small and large particles. The areal fraction of the amorphous regions increases with increasing c. See Fig. 2 of Ref.14 for the particle configurations for various c at $\sigma_2/\sigma_1 = 1.4$, where a crystal state was realized for $c = 0.02$ with large particles being distributed as point defects.

In this work, we carried out many simulation runs also for $c > 0.5$. For not very small c or $1 - c$, the system is divided into crystalline regions composed of the large particles and amorphpus layers composed of the two species. The areal fraction of the layers is decreased for relatively small c or $1 - c$. Figure 2 provides such an example for $c = 0.9$, where we display $D_j(t)$ at $t = 10^4$ in the left and the broken bonds and the displacement vectors

$$\Delta \boldsymbol{r}_j(t, \Delta t) = \boldsymbol{r}_j(t) - \boldsymbol{r}_j(t - \Delta t), \tag{16}$$

in the time interval $[10^4, 4\times10^4]$ with width $\Delta t = 3\times10^4$ in the right. In writing the displacements we pick up only mobile particles with $|\Delta \boldsymbol{r}_j| > 0.2$. At this composition percolation of the amorphous layers is attained. However, for $c = 0.95$, the layers

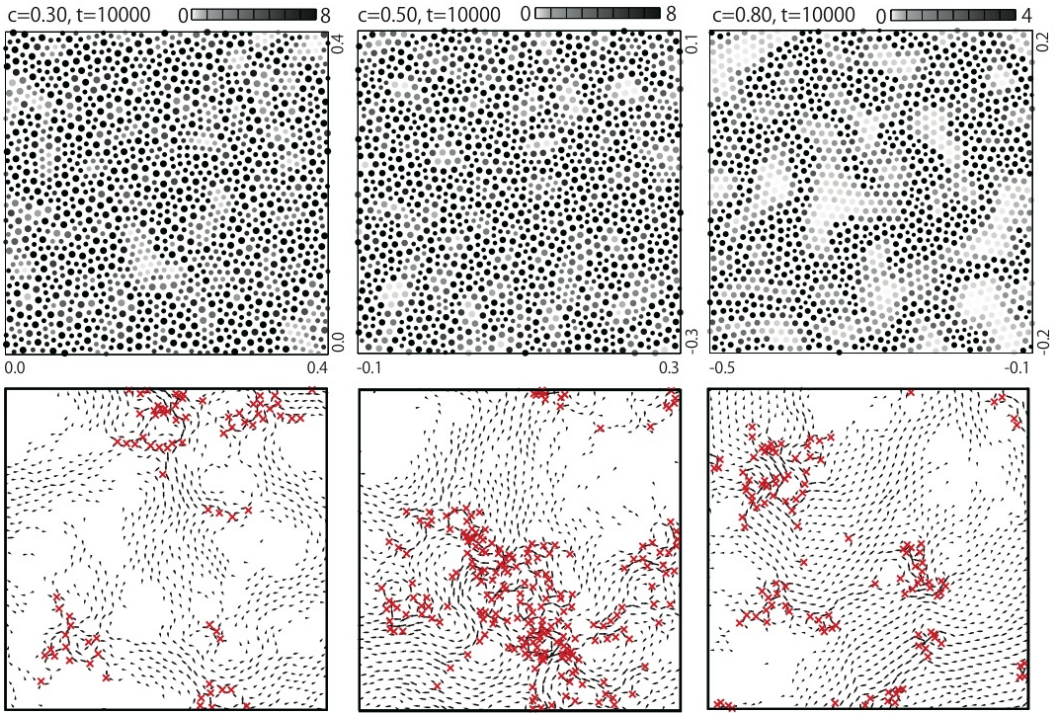

Fig. 4. (color online) Disorder variables $D_j(t)$ (upper plates), and broken bonds ($\times$) and displacement vectors for mobile particles with $|\Delta \boldsymbol{r}_j| > 0.2$ (lower plates) for $c = 0.3$, 0.5, and 0.8 with $\dot{\gamma} = 0$. For $c = 0.3$ and 0.5 the particles with $D_j > 8$ are written in black (upper plates).

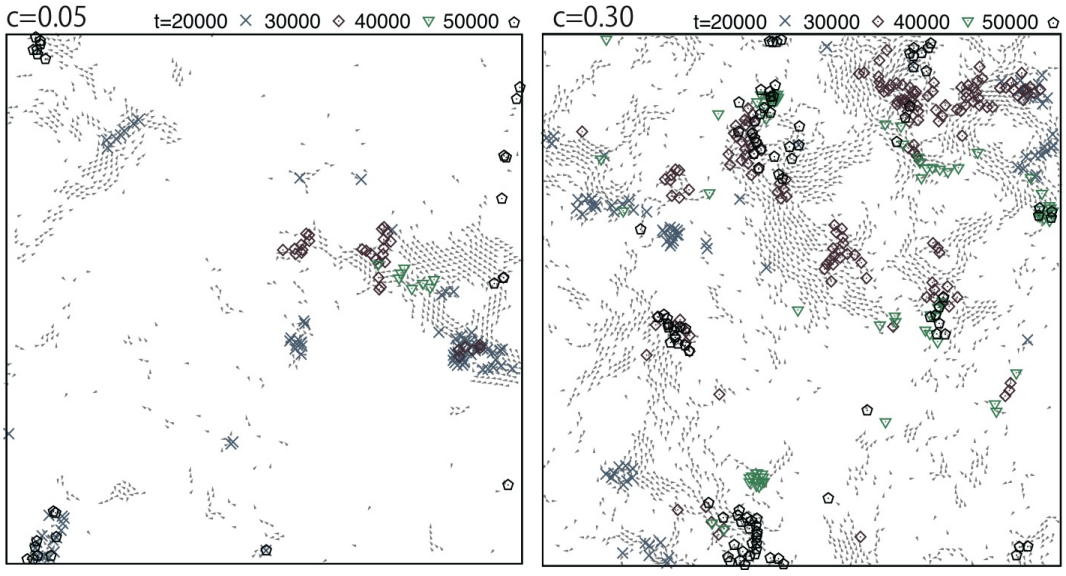

Fig. 5. (color online) Broken bonds and particle displacements with $|\Delta \boldsymbol{r}_j| > 0.2$ (arrows) in consecutive four time intervals with width $\Delta t = 10^4$ for $c = 0.05$ (left) and 0.3 (right) with $\dot{\gamma} = 0$ in the whole system. Shown is time evolution of the dynamic heterogeneity in polycrystal (left) and glass (right).

are broken into isolated clusters with various sizes, resulting in a crystal state with point defects (not shown here). In Fig. 2, the broken bonds are mostly created by the particle motions in the layers and are heterogeneously distributed. We also find coherent motions of crystalline domains surrounded by broken bonds at their grain boundaries. See the middle part at the bottom in the two panels for such an example. The patterns should be isotropic under the periodic boundary condition (on the average of many runs). Next, in Figs. 3 and 4, we show the same quantities for $c = 0.05$, 0.1, 0.15, 0.3, 0.5, and 0.8 to illustrate the crossover with increasing c. The system is in a well-defined polycrystal state for $c = 0.05$ and is highly disordered for $c = 0.3$ and 0.5. The structural heterogeneity in D_j and the dynamical one in the broken bonds and the displacements are both conspicuous for any c. Their correlation is obviously seen in the presence of small crystalline regions. This was illustrated in Ref. 14 in more expanded snapshots including the elusive case of glass.

Furthermore, in Fig. 5, we show time evolution of the broken bond distributions in four consecutive time intervals with width 10^4 in polycrystal at $c = 0.05$ and in glass at $c = 0.3$. The structural relaxation time τ_α is of order 10^5 at $c = 0.05$ and 10^4 at $c = 0.3$.[6] Here the clusters of the broken bonds mostly overlap or are adjacent to each other, resulting in aggregations of the broken bonds. Similar figures illustrating the heterogeneity evolution can be found in other papers also.[10),12),16),22)]

§4. Numerical results at $\dot\gamma = 10^{-4}$

We applied a simple shear flow with shear rate $\dot\gamma = 10^{-4}$. To this end, we divided the system into three regions.[31),56)] In the bulk region $-0.5L < x, y < 0.5L$, we initially placed particles with $N = 9000$. We added two boundary layers in the region $-0.6L < y < -0.5L$ at the bottom and in the region $0.5L < y < 0.6L$ at the top. In each layer, $N_b = 900$ particles with the same composition and size ratio were initially placed. They were attached to the layer by the spring potential,

$$u_j(\boldsymbol{r} - \boldsymbol{R}_j) = \frac{1}{2}K|\boldsymbol{r} - \boldsymbol{R}_j|^2, \tag{17}$$

where $\boldsymbol{R}_j = \boldsymbol{R}_j(t)$ are pinning points in the boundary layers dependent on t. The spring constant was set equal to $K = 20\epsilon\sigma_1^{-2}$. These bound particles also interacted with the neighboring bound and unbound particles with the common Lennard-Jones potentials in Eq. (5). The x component of $\boldsymbol{R}_j$ was moved as

$$X_j(t) = X_j(0) \pm \frac{1}{2}L\dot\gamma t. \tag{18}$$

We imposed the periodic boundary condition in the x direction. When $X_j(t) > L/2$ (or $X_j(t) < -L/2$) in the integration, $X_j(t)$ was decreased (or increased) by L. The unbound particles rarely penetrated into the boundary layers deeper than σ_1.

The unbound particles in the bulk regions obeyed the Newtonian equations of motion without thermostat. However, a Nosè-Hoover thermostat[62),63)] was attached

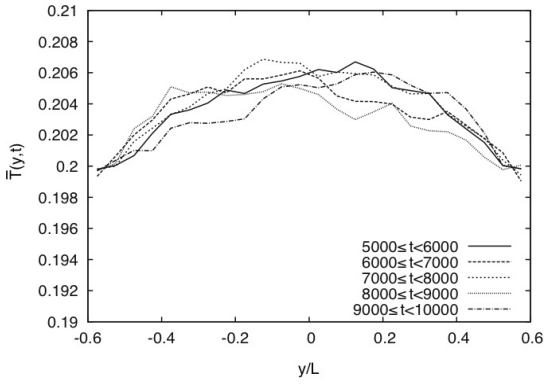

Fig. 6. Averaged temperature $\bar{T}(y,t)$ vs y/L with $\dot{\gamma} = 10^{-4}$ for $c = 0.05$, which is higher in the middle than the boundary value 0.2 only by a few %.

to each boundary layer independently. That is, the bound particles $j \in \mathcal{B}$ were governed by

$$m_j \ddot{\boldsymbol{r}}_j = -\frac{\partial}{\partial \boldsymbol{r}_j} U - \zeta_{\mathcal{B}} m_j (\dot{\boldsymbol{r}}_j - \boldsymbol{v}_{\mathcal{B}}), \quad (19)$$

where $\mathcal{B}$ denotes the top or the bottom. The boundary velocity $\boldsymbol{v}_{\mathcal{B}}$ is $(L\dot{\gamma}/2)\boldsymbol{e}_x$ at the top and $-(L\dot{\gamma}/2)\boldsymbol{e}_x$ at the bottom, where $\boldsymbol{e}_x$ is the unit vector along the x axis. For $\dot{\gamma} = 10^{-4}$ the boundary speed (~ 0.005) is much slower than the thermal velocity (~ 0.6). The two thermostat parameters, $\zeta_{\rm bot}$ at the bottom and $\zeta_{\rm top}$ at the top, obeyed

$$\frac{d}{dt}\zeta_{\mathcal{B}} = \frac{1}{\tau_{\rm NH}^2}\left[\frac{1}{N_b T}\sum_{j\in\mathcal{B}} \frac{m_j}{2}|\dot{\boldsymbol{r}}_j - \boldsymbol{v}_{\mathcal{B}}|^2 - 1\right]. \quad (20)$$

We set $\tau_{\rm NH} = 0.304$ and $T = 0.2$. For $\dot{\gamma} = 10^{-4}$, the local temperature was nearly homogeneous in the bulk region during plastic flow, as demonstrated in Fig. 6 for $c = 0.05$. Setting $\Delta t = 10^3$ and $\Delta y = L/20$, we define the averaged temperature by

$$\bar{T}(y,t) = \frac{1}{L\Delta y \Delta t}\int_{t-\Delta t}^{t} dt' \int_{y-\Delta y/2}^{y+\Delta y/2} dy' \int_{-L/2}^{L/2} dx' \epsilon_K(x',y',t'), \quad (21)$$

where $\epsilon_K(x,y,t) = \sum_j m_j |\dot{\boldsymbol{R}}_j - \dot{\gamma} y \boldsymbol{e}_x|^2 \delta(\boldsymbol{r} - \boldsymbol{R}_j)/2$ is the kinetic energy density.

We prepared the initial states as follows. First, we equilibrated the bulk and boundary regions independently without their mutual interactions. The particles in these regions interacted via the LJ potentials in Eq.(5) in a liquid state at $T = 2$ in a time interval of 10^3 under the periodic boundary condition along the x and y axes. Second, we quenched the system to $T = 0.2$ and further equilibrated it for a time interval of 10^3. Afterwards, we chose the particle positions in the boundary layers as the initial pinning points $\boldsymbol{R}_j(0)$ and introduced the spring potential of the bound particles and the LJ potentials between the bound and unbound particles. Third, we further waited for time interval of 5×10^3 until we detected no appreciable time evolution in various quantities. After this second low-temperature equilibration, we applied a shear flow with rate $\dot{\gamma} = 10^{-4}$ by sliding the pinning positions in the boundary layers with velocities $\pm\dot{\gamma}L/2$. We set $t = 0$ at the application of shear.

In Fig. 7, we show the broken bonds in five consecutive time intervals with width $5000 = 0.5/\dot{\gamma}$ in polycrystal at $c = 0.05$. Lines of the broken bonds represent plastic events created by dislocation gliding[48] or grain boundary sliding.[54] The former deformation mode is dominant at this small c, while the latter becomes increasing important with increasing c.[31),54] We can see that most of the slip lines are nearly parallel to the x or y axis. This is because the elastic energy of a slip is minimum in

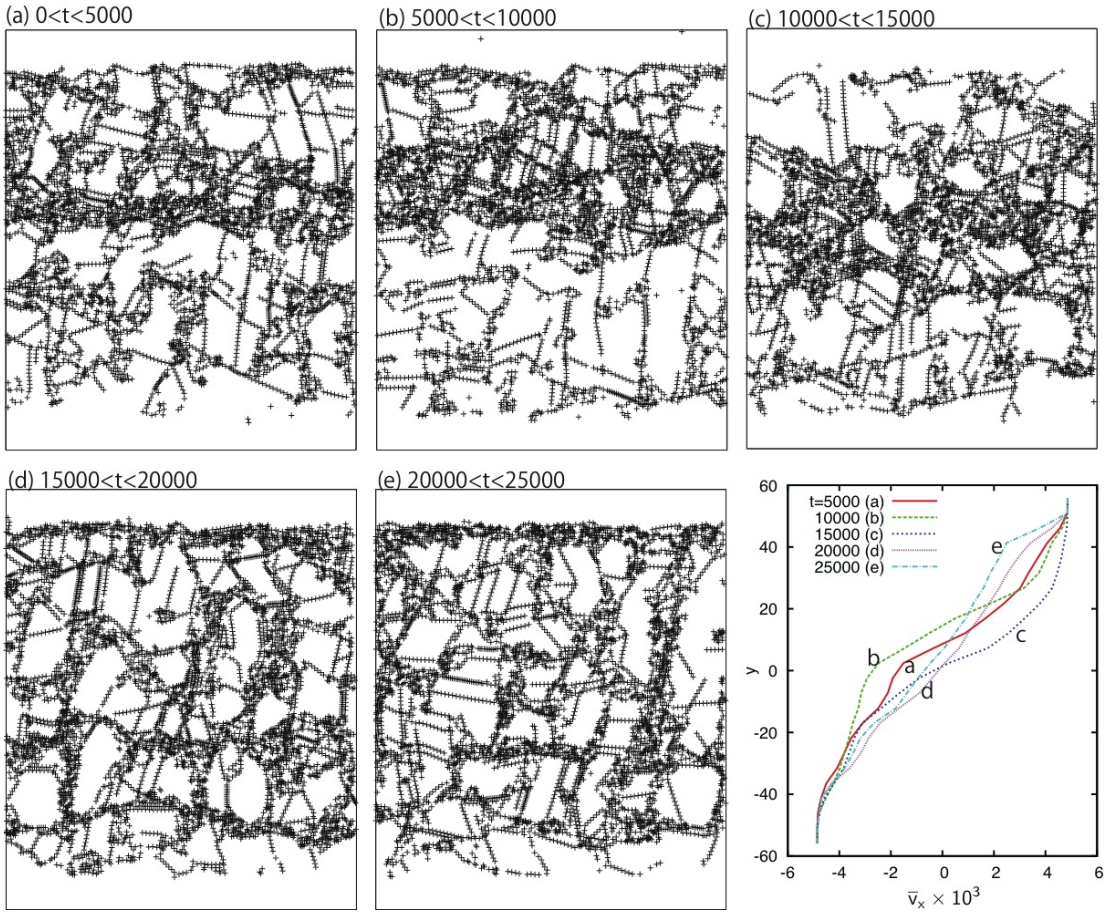

Fig. 7. Broken bonds in five consecutive time intervals with width $\Delta t = 5000 = 0.5/\dot{\gamma}$ in shear $\dot{\gamma} = 10^{-4}$ in polycrystal with $c = 0.05$. They form slip lines connecting grains. The top and bottom boundary layers are without broken bonds. Right bottom: averaged velocity $\bar{v}_x(y,t)$ defined by Eqs. (12) and (13) from the same data for these time intervals, which greatly changes in time and much deviates from the linear profile.

these directions in simple shear strain.[44] In the first three time intervals a thick band region extends over the system along the x axis in the upper part, but in the last two time intervals such large-scale bands are nonexistent. The right bottom panel displays the average velocity $\bar{v}_x(y,t)$ defined in Eqs. (12) and (13) with $\Delta t = 5 \times 10^3$, where the first three curves largely deviate from the linear profile $\dot{\gamma} y$ but the last two curves are nearly linear.

In Fig. 8, we show the same quantities in five consecutive time intervals with width $2500 = 0.25/\dot{\gamma}$ in glass at $c = 0.3$. Also in this case, the plastic deformations are highly heterogeneous, which still tend to be nearly parallel to the x or y axis. The chains of the broken bonds are shorter than in Fig. 7. That is, the slip lines do not much exceed the molecular size and the broken bonds are more randomly scattered than in polycrystal. As a result, the deviation of the averaged velocity $\bar{v}_x(y,t)$ from the linear form becomes small for $\Delta t \gtrsim 1/\dot{\gamma}$, while it is large for $\Delta t \lesssim 0.1/\dot{\gamma}$ (see Fig.

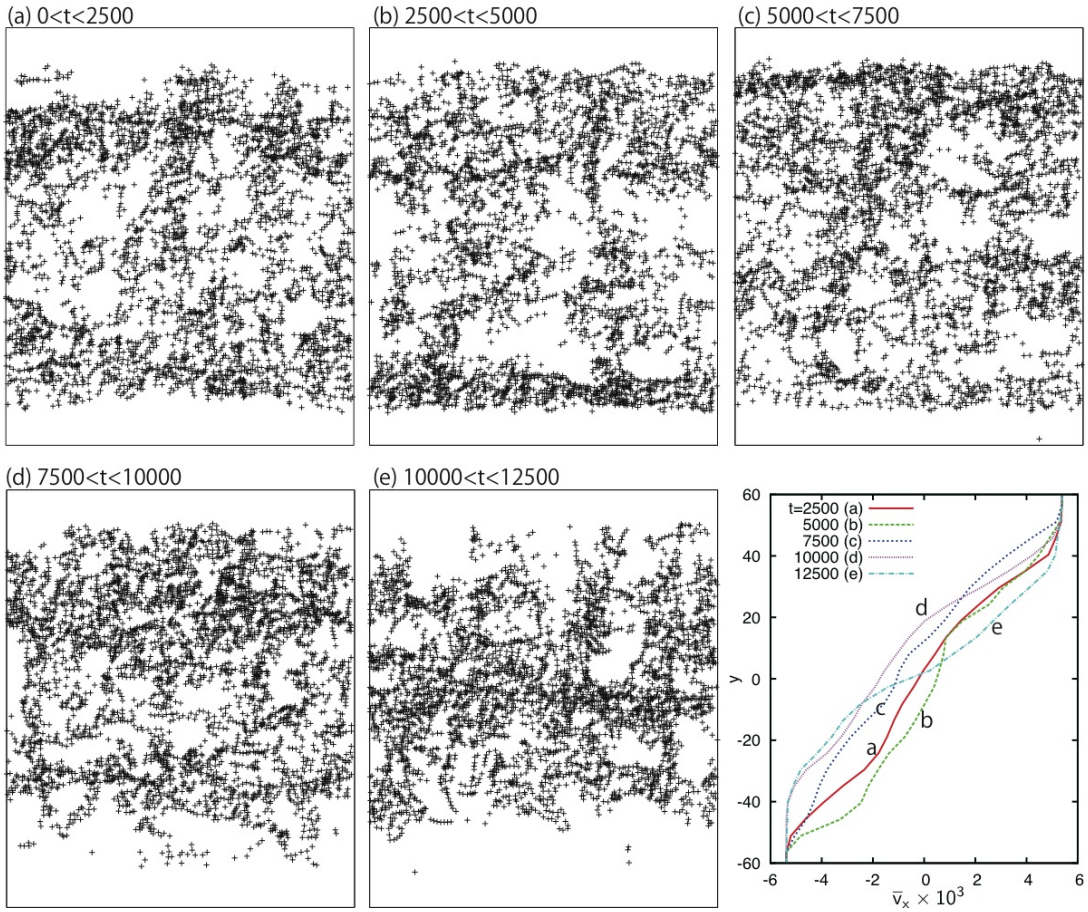

Fig. 8. Broken bonds in five consecutive time intervals with width $\Delta t = 2500 = 0.25/\dot{\gamma}$ in shear $\dot{\gamma} = 10^{-4}$ in glass with $c = 0.3$. Slip lines are short. Right bottom: averaged velocity $\bar{v}_x(y,t)$ from the same data for these time intervals.

9). In their long time simulation of sheared 2D glass, Furukawa *et al.*[30] realized transient shear bands equally in the flow and velocity-gradient directions with the Lees-Edwards boundary condition, while those parallel to the x axis more easily extend upto the system length in our simulation with the boundary layers.

Figure 9 illustrates the time-evolution of the dynamic heterogeneity in three consecutive time intervals with width $400 = 0.04/\dot{\gamma}$ in polycrystal at $c = 0.05$ and in glass at $c = 0.3$. We display the broken bonds in the left panels and the averaged velocity $\bar{v}_x(y,t)$ in the right panels. The width Δt here is made much shorter than in Figs. 7 and 8 to analyze the early stage of plastic deformations. Note that the transverse sound velocity $c_\perp$ is of order 5 (in units of σ/τ) and the acoustic traversal time $L/c_\perp$ is of order 20 in our system. (Plastic deformation dynamics on shoter time scales has been analyzed in our previous work.[31]) In the upper panels at $c = 0.05$, large-scale plastic deformations multiply occur in the same area, which extends over the system to form a shear band. On the other hand, in the lower panels at $c = 0.3$,

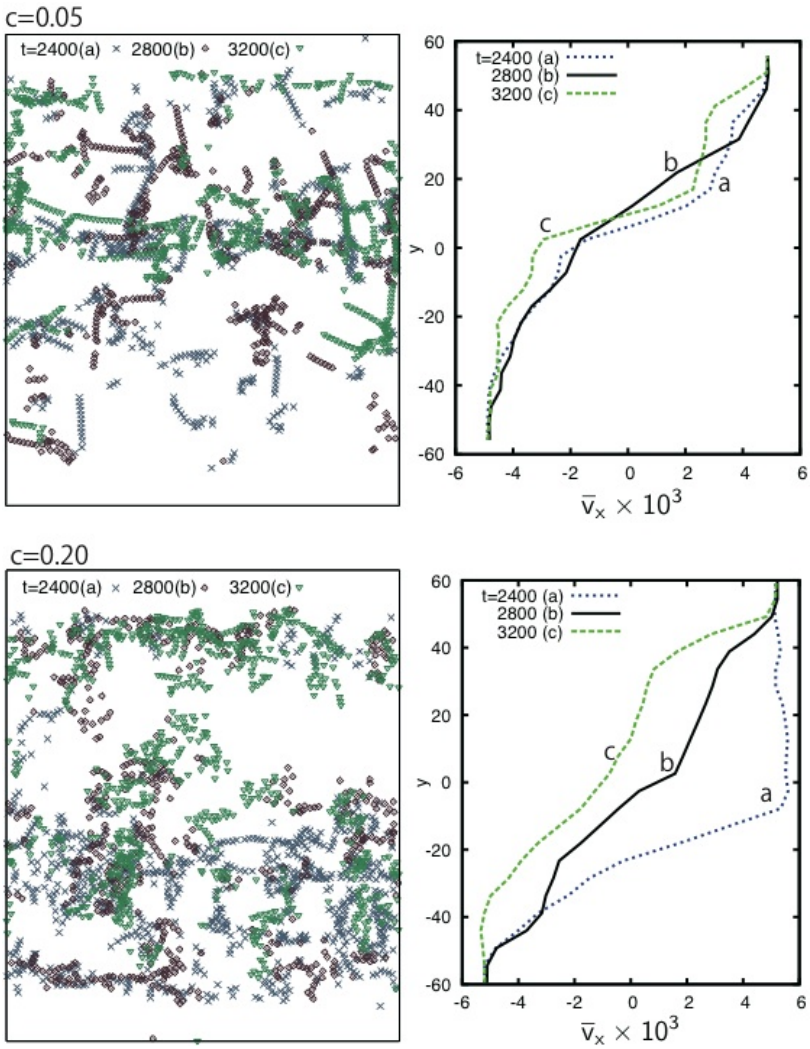

Fig. 9. (color online) Left: time evolution of bond breakage in three consecutive time intervals with width $\Delta t = 400 = 0.04/\dot{\gamma}$ in shear $\dot{\gamma} = 10^{-4}$. Right: averaged velocity $\bar{v}_x(y,t)$ for these time intervals much deviating from the linear profile. The system is in polycrystal with $c = 0.05$ (top) and in glass with $c = 0.2$ (bottom). Repeated occurrences of plastic events result in transient shear bands.

a large shear band is seen in the lower part in the first time interval, but large plastic deformations occur in the vertical direction in the second time interval and in the upper part in the horizontal direction in the third time interval. The life time of the shear bands is shorter in glass than in polycrystal.[31] In addition, the broken bond numbers ΔN_b in the whole system are 649, 551, and 614 for $c = 0.05$ and are 870, 589, and 761 for $c = 0.3$ in these time intervals in the chronological order. The time average of ΔN_b is of order $N\dot{\gamma}\Delta t (= 360$ here), which should be the case for any c as discussed at the end of Subsec.2.3.[31]

§5. Summary and remarks

We have examined the jammed particle configurations and the dynamic heterogeneity in 2D. Visualization of the disorder variable D_j gives information of the structural heterogeneity, while that of the bond breakage and the particle displacements discloses the presence of the dynamic heterogeneity. We have varied the composition c for $\sigma_2/\sigma_1 = 1.4$ and $T = 0.2\epsilon/k_B$. Summarizing our main results, we give some remarks below.

The particle configurations are unique in polycrystal and glass which are realized for not very small c or $1-c$ in our 2D model system. As in Figs. 2-4, small crystalline regions composed of one species of the particles are enclosed by percolated amorphous regions composed of the two species, where the amorphous regions form layers for relatively small c or $1-c$. For very small c or $1-c$ (not shown in this work), the layers break into small pieces to form a crystal with point defects. In rheology, these amorphous layers can serve as a lubricant in plastic flow,[31] within which the bond breakage occurs, reducing the viscosity than in crystal states.

In glass without shear, the particle configuration changes are thermally induced in the form of chains of broken bonds[10),22] or stringlike displacements.[11] They accumulate to form the dynamic heterogeneity on long times characterized by the correlation length ξ in Eq.(1).[10),16),31] In Figs. 2-4, we have added more evidences for these dynamical processes. To show the relationship between the structural and dynamical heterogeneities, we have presented the snapshots of the disorder variable D_j and those of the bond breakage and the displacements (see Fig. 2 in Ref.14 also). In Fig. 5, we have visualized the time evolution of the dynamic heterogeneity on the time scale of 10^4, which demonstrates correlated occurrences of mesoscopic structural changes. This tendency is related to the mesoscopic heterogeneity in the elastic moduli.[20),21] In addition, in Fig. 4, the structural relaxation is even slower in polycrystal than in glass, where the particles around the grain boundaries (in the amorphous layers) are relatively mobile than those within the crystalline grains.[14]

In shear flow with $\dot\gamma = 10^{-4}$, we have visualized large-scale heterogeneity in the bond breakage in Figs. 6-8. The averaged velocity $\bar v_x(y,t)$ deviates from the linear profile with formation of shear bands. Here $\Delta t = 0.5/\dot\gamma$ for $c = 0.05$ in Fig. 7, $\Delta t = 0.25/\dot\gamma$ for $c = 0.3$ in Fig. 8, and $\Delta t = 0.04/\dot\gamma$ for $c = 0.05$ and 0.3 in Fig. 9. These figures illustrate how the plastic deformations under shear evolve on various time scales. For any c, plastic deformations extend over longer distances nearly in the x or y axis as in Fig. 9. Such plastic events often accumulate to form transient shear bands as in Figs. 7-8. They occur to release the elastic energy at high strain as discussed in Sec.I. See Refs. 27 and 28 for more discussions on the anisotropic, hierarchical dynamics under shear. In the early work by Yamamoto and one of the present authors,[22] the shear-induced structural change was analyzed on the basis of Eq.(2) and the broken-bond structure factor $S_b(k)$ in Eq.(1) was calculated for $\Delta t = 0.05\tau_b \cong 0.5\tau_\alpha$ without and with shear, but the shear band formation on large scales was beyond its scope.

A variety of complex problems of binary particle systems remain mostly unexplored. We mention some of them. (i) When the size ratio σ_2/σ_1 is increased

from unity, intriguing crossovers are expected in the particle configurations and the dynamics. For example, at $c = 0.5$, proliferation of defects occurs abruptly around $\sigma_2/\sigma_1 \cong 1.2$.[6),14)] (ii) Furthermore, with changing the pair potentials, tendency to phase sparation can be enhanced, where small crystalline regions should become more disinct or nucleation of crystal domains should become realizable in an amorphous matrix. (iii) Some essential aspects of the glass problem should be common in 2D and 3D. However, in 3D, the problem is much more complicated and visualization of configuration changes is more difficult. We have not yet understood the differences in 2D and 3D in depth. (iv) In addition, the melting and crystallization in binary mixtures have not yet been well investigated, where essentially different pictures arise in 2D and 3D. We have recently recognized surprising complexity of the 2D melting even in one component systems.[61)] That is, marked heterogeneities emerge both in the structural disorder and in the dynamics in the hexatic phase,[60)] where mesoscopic liquidlike and crystalline regions coexist as thermal fluctuations without distinct interfaces. Understanding the dynamics of 2D melting is still at the beginning despite numerous papers on static properties.

Acknowledgements

The authors would like to thank Akira Furukawa and Ryoichi Yamamoto for valuable discussions. Some of the numerical calculations were carried out on Altix 3700B at ISSP Supercomputer Center, Univ. of Tokyo. This work was supported by Grants-in-Aid for scientific research on Priority Area "Soft Matter Physics" and the Global COE program "The Next Generation of Physics, Spun from Universality and Emergence" of Kyoto University from the Ministry of Education, Culture, Sports, Science and Technology of Japan.

References

1) E. Dickinson and R. Parker, Chem. Phys. Lett. **79** (1981), 578.
2) L. Bocquet, J.P. Hansen, T. Biben, and P. Madden, J. Phys.: Condens. Matter **4** (1992), 2375.
3) C.N. Likos and C.L. Henry, Phil. Mag. B **68** (1993), 85.
4) W. Vermölen and N. Ito, Phys. Rev. E **51** (1995), 4325.
H. Watanabe, S. Yukawa, and N. Ito, Phys. Rev. E **71** (2005), 016702.
5) M. R. Sadr-Lahijany, P. Ray, and H. E. Stanley, Phys. Rev. Lett. **79** (1997), 3206.
6) T. Hamanaka and A. Onuki, Phys. Rev. E **74** (2006), 011506.
7) K. Maeda and S. Takeuchi, Phys. Stat. Sol. **49** (1978), 685.
8) T. Muranaka and Y. Hiwatari, Phys. Rev. E **51** (1995), 2735(R).
9) M. M. Hurley and P. Harrowell, Phys. Rev. E **52** (1995), 1694.
10) R. Yamamoto and A. Onuki, J. Phys. Soc. Jpn., **66** (1997) ,2545.
11) W. Kob, C. Donati, S. J. Plimton, P. H. Poole, and S. C. Glotzer, Phys. Rev. Lett. **79** (1997), 2827.
12) B. Doliwa and A. Heuer, J. Non-Cryst. Solids **307**-310 (2002), 32.
13) A. Widmer-Cooper and P. Harrowell, Phys. Rev. Lett. **96** (2006), 185701.
14) T. Hamanaka and A. Onuki, Phys. Rev. E **75** (2007), 041503.
15) T. Kawasaki, T. Araki, and H. Tanaka, Phys. Rev. Lett. **99** (2007), 215701.
16) R. Candelier, A. Widmer-Cooper, J. K. Kummerfeld, O. Dauchot, G. Biroli, P. Harrowell, and D.R. Reichman, arXiv.org, cond-mat, arXiv:0912.0193.
17) H. Sillescu, J. Non-Cryst. Solids **243**, 81 (1999).
18) M. D. Ediger, Annu. Rev. Phys. Chem. **51**, 99 (2000).

19) R. Yamamoto and A. Onuki, Phys. Rev. Lett. **81** (1998), 4915.
20) K. Yoshimoto, T. S. Jain, K. Van Workum, P. F. Nealey, and J. J. de Pablo, Phys. Rev. Lett. **93** (2004), 175501.
21) M. Tsamados, A. Tanguy, C. Goldenberg, and J.-L. Barrat, Phys. Rev. E **80** (2009), 026112.
22) R. Yamamoto and A. Onuki, Europhys. Lett. **40** (1997), 61; Phys. Rev. E **58** (1998), 3515; J. Phys. Condens. Matter **29** (2000), 6323.
23) L. Angelani, G. Ruocco, F. Sciortino, P. Tartaglia, and F. Zamponi, Phys. Rev. E **66** (2002), 061505.
24) M. Fuchs and M. E. Cates, Phys. Rev. Lett. **89** (2002), 248304.
K. Miyazaki, D.R. Reichman, Phys. Rev. E **66** (2002), 050501(R).
25) F. Varnik, L. Bocquet, J.-L. Barrat, and L. Berthier, Phys. Rev. Lett. **90** (2003), 095702.
26) L. Berthier, J. Phys. Condens. Matter **15**, S933 (2003).
27) A. Tanguy, F. Leonforte, and J.-L. Barrat, Eur. Phys. J. E **20** (2006), 355.
28) A. Lemaitre and C. Caroli, Phys. Rev. E **76** (2007), 036104.
29) Y. Shi, M. B. Katz, H. Li, and M. L. Falk, Phys. Rev. Lett. **98** (2007), 185505.
30) A. Furukawa, K. Kim, S. Saito, and H. Tanaka, Phys. Rev. Lett. **102**, 016001 (2009).
31) H. Shiba and A. Onuki, arXiv.org, cond-mat, arXiv:0911.4922.
32) T. Okuzono and K. Kawasaki, Phys. Rev. E **51** (1995), 1246.
33) D.J. Durian, Phys. Rev. E **55** (1997), 1739.
S. A. Langer and A. J. Liu, J. Phys. Chem. B **101** (1997), 8667.
34) B. Miller, C.O'Hern and R.P. Behringer, Phys. Rev. Lett. **77** (1996), 3110.
35) O. Dauchot, G. Marty, and G. Biroli, Phys. Rev. Lett. **95** (2005), 265701.
36) P. Olsson and S. Teitel, Phys. Rev. Lett. **99** (2007), 178001.
T. Hatano, Phys. Rev. E **79** (2009), 050301(R).
37) J.H. Li and D.R. Uhlmann, J. Non-Cryst. Solids **3** (1970), 127.
38) J.H. Simmons, R.K. Mohr, and C.J. Montrose, J. Appl. Phys. **53** (1982), 4075.
39) A. Onuki, J. Phys. C **9** (1997), 6119.
40) Y. Shi and M. L. Falk, Phys. Rev. B **73** (2006), 214201.
41) C. E. Maloney and M. O. Robbins, J. Phys.: Condens. Matter **20** (2008), 244128.
42) N. P. Bailey, J. Schiϕtz, and K. W. Jacobsen, Phys. Rev. B **73** (2006), 064108.
43) V.V. Bulatov and A.S. Argon, Model. Simul. Mater. Sci. Eng. **2** (1994), 167.
44) A. Onuki, Phys. Rev. E **68** (2003), 061502.
45) Jing Li, F. Spaepen and T.C. Hufnagel, Phil. Mag. A **82** (2002), 2623.
46) Q. Wei, D. Jia, K. T. Ramesh, and E. Ma Appl. Phys. Lett. **81** (2002), 1240.
47) C. A. Schuh, T. C. Hufnagel , and U. Ramamurty Acta Materialia **55** (2007), 4067.
48) J. Friedel, *Dislocations* (Pergamon, New York, 1954).
49) M.-C. Miguel, A. Vespignani, S. Zapperi, J. Weiss, and Jean-Robert Grassok, Nature **410** (2001), 667.
M. Zaiser, Adv. Phys. **55**, 185 (2006).
50) D. M. Dimiduk, C. Woodward, R. LeSar, and M. D. Uchic, Science **312** (2006), 1188.
51) B. Devincre and L. P. Kubin Mater. Sci. Eng. A **234-236** (1997), 8.
V. Bulatov, F. F. Abraham, L. Kubin, B. Devincre and S. Yip, Nature **391** (1998), 669.
52) A. Minami and A. Onuki, Phys. Rev. B **70** (2004), 184114; Acta Mater. **55** (2007), 2375.
53) V. Yamakov, D. Wolf, S. R. Phillpot, A. K. Mukherjee, and H. Gleiter, Nature Materials **3** (2004), 43.
54) S. Yip, Nature Mater. **3** (2004), 11.
55) H. Zhang, D. J. Srolovitz, J. F. Douglas, and J. A. Warren, Phys. Rev. B **74** (2006), 115404.
56) T. Hamanaka, H. Shiba, and A. Onuki, Phys. Rev. E **77** (2008), 042501.
57) F. Spaepen, Acta Metall. **25** (1977), 407.
58) A.S. Argon, Acta Metall. **27** (1979), 47.
59) M. L. Manning, J. S. Langer, and J. M. Carlson, Phys. Rev. E **76** (2007), 056106.
60) B.I. Halperin and D. R. Nelson, Phys. Rev. Lett. **41** (1978), 121.
61) H. Shiba, A. Onuki and T. Araki, EPL **86** (2009), 66004.
62) S. Nosè, Prog. Theor. Phys. Suppl. **103** (1991), 1.
63) W.G. Hoover, *Computational Statistical Mechanics*, (Elsevier, Amsterdam,1991).